J. Fluid Mech. (1980), *vol.* 100, *part* 1, *pp.* 87–110
Printed in Great Britain

Subgrid modelling studies with Burgers' equation

By M. D. LOVE

Department of Nuclear Engineering, Queen Mary College,
Mile End Road, London E1 4NS

(Received 15 November 1978 and in revised form 4 February 1980)

Burgers' equation, a one-dimensional analogue of the Navier–Stokes equation, has been solved numerically in full detail at high (equivalent) Reynolds numbers. These fine-mesh solutions have been used to study the dynamics of the Burgers' equation analogue of three-dimensional turbulence and in particular the drain of energy from the large to the small structures.

The equation has also been solved on a coarse mesh, using various forms of subgrid model. The solutions so derived have been compared with filtered solutions of the same problem on a fine mesh. In this way it has been possible to test directly the performance of subgrid models at high Reynolds numbers, a test which cannot be made on the Navier–Stokes equations themselves.

With proper choice of the parameters, the performance of the subgrid models is very satisfactory.

1. Introduction

The great range of eddy sizes in a high-Reynolds-number flow means that for such flows it still is and may always be impossible to compute the detailed motions of all the length scales present (Corrsin 1961). Large-eddy simulations provide a way round this impasse: they give the detailed time-dependent motions of the large eddies only. They smooth over the details of the small dissipation eddies, and thus for a high-Reynolds-number flow, reduce the range of eddy sizes to a manageable level.

This reduction in the range of eddy sizes is achieved by working with the space-averaged (filtered) Navier–Stokes equations. Large-eddy simulations are simply numerical solutions to these equations. Unfortunately in deriving the space-averaged Navier–Stokes equations terms that involve the small eddies still appear. These terms represent the drain of energy from the large eddies to the small eddies, and cannot be ignored. This means that if the detailed motions of the small eddies are not to be included in the calculation, ways must be found to represent this drain that do not depend on a detailed description of the small eddies. The solution is to replace the terms by a sub-grid model that involves only the detailed motions of the large eddies.

Subgrid models then are necessary in large-eddy simulations in order to close the calculations. Although there are strong reasons for believing subgrid models to be more universal than one-point closure models (Ferziger 1976), it appears that the choice of subgrid model can nevertheless greatly influence the success of a large-eddy simulation. A wide variety of subgrid models, filters, boundary conditions, and finite-difference schemes have been tried. Despite this neither the optimum choice of subgrid

0022-1120/80/4541-2130 $02.00

model nor the reasons for making the choice are clear. This is because for high-Reynolds-number turbulent flows exact non-trivial solutions to the Navier–Stokes equations do not exist. Also for such flows the complex interaction between the physics and numerics means that in a large-eddy simulation it is very difficult to unscramble the effects of the various processes present. Consequently in this article we attempt to examine the nature and effectiveness of subgrid modelling procedures by seeking numerical solutions to the Burgers' equation

$$\frac{\partial}{\partial t}u(x,t)+u\frac{\partial}{\partial x}u-\nu\frac{\partial^2}{\partial x^2}u=f(x,t), \tag{1}$$

subject to the boundary conditions

$$u(x,t)=u(x+L,t) \quad \text{for} \quad 0\leqslant x\leqslant L.$$

Here $f(x,t)$ is a driving force.

Burgers' equation is a one-dimensional analogue of the Navier–Stokes equations. Its one-dimensional character allows us to sidestep the difficulties encountered in studying the effectiveness of subgrid modelling procedures by numerical calculations on the high-Reynolds-number Navier–Stokes equations. For Burgers' equation all scales of motion can be modelled in the computation, even if the Reynolds number is very high. These 'exact' solutions can be compared with coarse-mesh or large-eddy simulation solutions, and this affords a precise method for testing the performance of the large-eddy simulation technique at high Reynolds numbers.

The investigation is in two parts. First we solve equation (1) on a fine mesh with periodic boundary conditions and with all length scales fully resolved: the results of these calculations are designated exact. They allow us to explore the exact dynamics of Burgers' equation and to demonstrate that there are many qualitative similarities between its solutions and those of Navier–Stokes turbulence. In particular they confirm previous findings (Kraichnan 1968; Hosokawa & Yamamoto 1975) that for Burgers' model turbulence the large and small eddies are statistically independent and separated in wavenumber space by a characteristic inertial range. We then filter the exact solutions and explore both the dynamics of the large-scale flow structures and the properties of the subgrid energy-drain terms. The results of these calculations confirm Burgers' model turbulence as a useful vehicle for exploring the effectiveness of subgrid modelling techniques. They also justify the second stage of the investigation in which we attempt to reproduce, using the large-eddy simulation technique, the dynamics of the large-scale flow structures as observed in the exact calculations. This in turn permits us to explore both the optimum choice of subgrid model and the propagation of error.

The calculations reported below are for three flow situations: these are the free decay of an ensemble of shock fronts, a travelling wave solution, and a stochastically forced ensemble of shock fronts. Of these, the second represents a simple flow situation, whose study allows us to isolate and investigate in detail the cause of spectral distortions. The other two represent more complex-flow situations which, since they are more akin to real flows, provide a more rigorous test of subgrid modelling technique. Details of the numerical techniques used for this investigation are available on

request; some of the preliminary findings of this investigation have been presented elsewhere (Love & Leslie 1977).

2. Mathematical formation

2.1. *The filtered equation of motion*

In applying the large-eddy simulation technique to Burgers' model turbulence it is first necessary to derive an equation of motion for the large-scale (grid-scale) velocity components. The nonlinear nature of Burgers' equation means that there is a continuous range of eddy sizes and that consequently there is no natural division of the flow into large and small eddies. The same is true for Navier–Stokes turbulence. We therefore effect the division following Leonard (1974) by defining grid-scale variables according to

$$\bar{g}(x,t) = \int_{\text{space}} G(x,x')\,g(x',t)\,dx' \tag{2}$$

and subgrid variables by

$$g'(x,t) = g(x,t) - \bar{g}(x,t). \tag{3}$$

Here G denotes a filter function with characteristic length Δ. Following the recommendations of Kwak, Reynolds & Ferziger (1975) we adopt for this work the Gaussian filter

$$G(z) = (6/\pi\Delta^2)^{\frac{1}{2}} \exp(-6z^2/\Delta^2), \tag{4}$$

where

$$z = x - x'.$$

In using this filter, we recognize that there is no sharp separation between large and small eddies. Instead it gradually attenuates the small-scale structures.

Filtering equation (1) according to (2) we obtain

$$\frac{\partial}{\partial t}\bar{u}\,(x,t) + \frac{\partial}{\partial x}\left(\frac{\bar{u}^2}{2} + R\right) - \nu\frac{\partial^2}{\partial x^2}\bar{u} = \bar{f}(x,t) \tag{5}$$

where

$$R = \tfrac{1}{2}(\overline{\bar{u}\bar{u}} - \bar{u}\bar{u}) + \overline{\bar{u}u'} + \tfrac{1}{2}\overline{u'u'} \tag{6}$$

denotes the residual stress. The first term in (6) is called the resolvable scale or Leonard stress since it does not involve the subgrid component u' explicitly.

The dependent variables in (5) vary smoothly over lengths of $O(\Delta)$. This means that in seeking to solve (5) by numerical methods a relatively coarse mesh with interval h, where h is of $O(\Delta)$, can be used. Without filtering h would need to be smaller than the smallest dissipation eddy, thus demanding the use of a very fine mesh: in the case of a three-dimensional flow it would not be possible to accommodate such a mesh on existing computers. The price paid for making the calculation fit onto a coarse mesh in this matter is that the u' are unknown. To close the filtered equations of motion those terms which involve u' must be approximated by expressions that only involve $\bar{u}$. From the physical viewpoint this amounts to replacing the terms that involve u' by a subgrid model which represents the interaction between the large and small eddies with terms that depend only on the detailed motions of the large eddies.

2.2. *Specification of subgrid models*

The models are first presented as mathematical constructs; their performance is then subsequently investigated and analysed. We consider four subgrid models. They are all one-dimensional analogues of subgrid models used elsewhere in the simulation of homogeneous Navier–Stokes turbulence. The first assumes that the residual stress term in (5) behaves as though it were due to molecular viscosity: using this analogy we simply define a turbulent viscosity ν_{T1} by

$$R = -\nu_{T1}\frac{\partial}{\partial x}\bar{u} \tag{7}$$

and then assume a functional form for ν_{T1}. We return later to the complete specification of ν_{T1} (see equation (14)).

Model 2 is a variant of this basic model. It relies on the approximation

$$\bar{g}(x,t) = g(x,t)\int_{\text{space}} G(z)\,dz + \frac{1}{2}\frac{\partial^2}{\partial x^2}g(x,t)\int_{\text{space}} z^2 G(z)\,dz + O(\Delta^4), \tag{8}$$

which, for the Gaussian filter specified by (4), simplifies to

$$\bar{g}(x,t) = g(x,t) + \frac{\Delta^2}{24}\frac{\partial^2}{\partial x^2}g(x,t) + O(\Delta^4). \tag{9}$$

Using this expansion procedure we approximate the first term on the right-hand side of (6) by

$$[\overline{\bar{u}^2} - \bar{u}^2] = \frac{\Delta^2}{24}\frac{\partial^2}{\partial x^2}\bar{u}^2 + O(\Delta^4) \tag{10}$$

and then assume the remainder of the residual stress term in (5) behaves as though it were due to a molecular viscosity. We accordingly define the turbulent viscosity ν_{T2} by

$$R = \frac{\Delta^2}{48}\frac{\partial^2}{\partial x^2}\bar{u}^2 - \nu_{T2}\frac{\partial}{\partial x}\bar{u}. \tag{11}$$

This completes model 2: again we leave the detailed specification of ν_{T2} until later (see equation (14)).

Models 3 and 4 define the turbulent viscosities ν_{T3} and ν_{T4} by

$$R = \frac{\Delta^2}{24}\left[\frac{\partial\bar{u}}{\partial x}\right]^2 - \nu_{T3}\frac{\partial\bar{u}}{\partial x} \tag{12}$$

and

$$\frac{\partial}{\partial x}\left[\frac{\overline{\bar{u}\bar{u}}}{2} + R\right] = [\bar{u}(x+h) + \bar{u}(x) + \bar{u}(x-h)]\,[\bar{u}(x+h) - \bar{u}(x-h)]/6h - \frac{\partial}{\partial x}\left(\nu_{T4}\frac{\partial}{\partial x}\bar{u}\right). \tag{13}$$

These models are analogous to subgrid models used elsewhere (see Ferziger 1976) in the simulation of Navier–Stokes turbulence. There is no simple physical concept such as eddy viscosity embodied in the construction of either of these models. Model 3 can be

derived from model 2 if the expansion procedure of equation (9) is applied to the first two terms appearing on the right-hand side of equation (6). Such an expansion is however mathematically indefensible since the u' are not smoothly varying over lengths of $O(\Delta)$. Model 4 follows from a detailed examination of the round-off errors appearing in a second-order energy-conserving finite-difference approximation to the term $\partial\overline{u^2}/\partial x$ (see equation (34)). In short both models 3 and 4 are nothing other than guesses giving an alternative to the standard eddy viscosity models. Model 3 has the advantage over model 2 of involving a lower order differential, which simplifies the treatment of boundary regions. Model 4 is particularly easy to implement from a numerical view point.

The substitution of any of equations (7), (11) or (13) into (5) gives a closed equation of motion for the grid scale velocity field once the form of the ν_{Ti} is specified. We effect the closure by assuming

$$\nu_{Ti} = c_i^2 \Delta^2 \overset{w}{\overline{|\partial\overline{u}/\partial x|}} \tag{14}$$

where c_i is a constant and $\overset{w}{\overline{|\partial\overline{u}/\partial x|}}$ denotes the average over a length w of the quantity $|\partial\overline{u}/\partial x|$. In the limit as $w \to 0$ equation (14) tends to the one-dimensional equivalent of the Smagorinsky–Lilly subgrid model (Smagorinsky 1963; Lilly 1966, 1967). In the limit as $w \to L$ it tends to the direct-interaction subgrid model investigated by Leslie & Quarini (1979; see also Love & Leslie 1977).

2.3. *Energy balance in the filtered equation of motion*

The equation of motion for the energy per unit volume in the exact and grid-scale fields is obtained by multiplying (1) and (5) throughout by u and $\overline{u}$ respectively, and then averaging the ensuing raw-energy equation over an ensemble of realizations of the flow field. The result for a homogeneous flow is

$$-\frac{d}{dt}\langle \tfrac{1}{2}u^2 \rangle = \epsilon_{\mathrm{mv}} - \langle uf \rangle \tag{15}$$

and

$$-\frac{d}{dt}\langle \tfrac{1}{2}\overline{u}^2 \rangle = \bar{\epsilon}_{\mathrm{rs}} + \bar{\epsilon}_{\mathrm{sgs}} + \bar{\epsilon}_{\mathrm{mv}} - \langle \overline{u}\bar{f} \rangle, \tag{16}$$

where $\langle\,\rangle$ denotes the operation of averaging over an ensemble of realizations. In equation (16) the grid-scale dissipation is seen to comprise three components, the resolvable scale component $\bar{\epsilon}_{\mathrm{rs}}$, the subgrid scale component $\bar{\epsilon}_{\mathrm{sgs}}$, and the molecular viscosity component $\bar{\epsilon}_{\mathrm{mv}}$. These are defined as

$$\bar{\epsilon}_{\mathrm{rs}} = \frac{1}{2}\left\langle \overline{u}\frac{\partial}{\partial x}(\overline{\overline{u}^2} - \overline{u}^2) \right\rangle \tag{17}$$

$$\begin{aligned}\bar{\epsilon}_{\mathrm{sgs}} &= \left\langle \overline{u}\frac{\partial}{\partial x}\overline{\overline{u}u'} \right\rangle + \frac{1}{2}\left\langle \overline{u}\frac{\partial}{\partial x}\overline{u'^2} \right\rangle \\ &= \bar{\epsilon}_{\mathrm{rs:sgs}} + \bar{\epsilon}_{\mathrm{sgs:sgs}}\end{aligned} \tag{18}$$

and

$$\bar{\epsilon}_{\mathrm{mv}} = -\nu\left\langle \overline{u}\frac{\partial^2}{\partial x^2}\overline{u} \right\rangle. \tag{19}$$

In equation (15) ϵ_{mv} is the whole of the molecular-viscous dissipation. It will be seen from these equations that the crucial difference between the energy balance in the exact field and the grid-scale field is that in the former the nonlinear terms are energy conserving and therefore vanish whereas in the latter they are responsible for the drain of energy from the flow field. If we consider the contribution of the subgrid drain term to the energy balance, model 1 may be written as

$$\bar{\epsilon}_{\nu T} = \bar{\epsilon}_{\mathrm{rs}} + \bar{\epsilon}_{\mathrm{sgs}} \tag{20}$$

model 2 as

$$\bar{\epsilon}_{\nu T} = \bar{\epsilon}_{\mathrm{sgs}}$$

$$\bar{\epsilon}_{\mathrm{rs}} = \frac{\Delta^2}{48}\left\langle \overline{u}\,\frac{\partial^2}{\partial x^2}\,\overline{u}^2 \right\rangle \tag{21}$$

model 3 as

$$\bar{\epsilon}_{\nu T} = \bar{\epsilon}_{\mathrm{sgs;\,sgs}}$$

$$\bar{\epsilon}_{\mathrm{rs}} + \bar{\epsilon}_{\mathrm{rs;sgs}} = -\frac{\Delta^2}{24}\left\langle \overline{u}\left[\frac{\partial}{\partial x}\,\overline{u}\right]^2 \right\rangle. \tag{22}$$

Here

$$\bar{\epsilon}_{\nu T} = -\left\langle \overline{u}\,\frac{\partial}{\partial x}\left(\nu_{Ti}\,\frac{\partial}{\partial x}\,\overline{u}\right)\right\rangle \tag{23}$$

denotes the rate at which energy is dissipated through the eddy viscosity closure assumption. In model 4 the relationship between the different terms appearing in the subgrid model and the components of the grid-scale dissipation is not clear.

Finally we note that

$$\bar{E}(k,t) = \langle \overline{u}(k,t)\,\overline{u}(-k,t)\rangle \tag{24}$$

($\overline{u}(k,t)$ being the Fourier transform of $\overline{u}(x,t)$) satisfies the equation

$$\left(\frac{d}{dt} + 2\nu k^2\right)\bar{E}(k,t) = T(k,t) + P(k,t); \tag{25}$$

P and T represent the effects of production and of net outward inertial transfer. Equation (25) is of course identical with the energy-balance relation for the Navier–Stokes equations. The term $T(k,t)$ in equation (25) is derived from the term $\partial[\frac{1}{2}\overline{u}^2 + R]/\partial x$ in equation (5), while $P(k,t)$ is derived from the term $\bar{f}(x,t)$. The contribution of the residual stress R to $T(k,t)$ means that $T(k,t)$ is not energy conserving.

3. Fine-mesh calculations

3.1. *Definition of length scales and the numerical model*

Fine-mesh calculations were performed for two flow configurations: a freely decaying ensemble of shock fronts, and a stochastically forced ensemble of shock fronts. We put equation (1) in dimensionless form by scaling all lengths with L_0 and all times with $T_0 = L_0/U_0$, and then compute the time evolution of $u(x,t)$. Here $L_0 = 2/K_{\max}$, where $K_{\max}^{-1}$ is the wavelength at which $E(k, t=0)$ reaches its maximum and $E_0 = \frac{1}{2}\overline{u}_0^2$ denotes the mean energy per unit length of the flow. The Reynolds number defined by

$$Re = L_0 U_0/\nu|_{t=0} \tag{26}$$

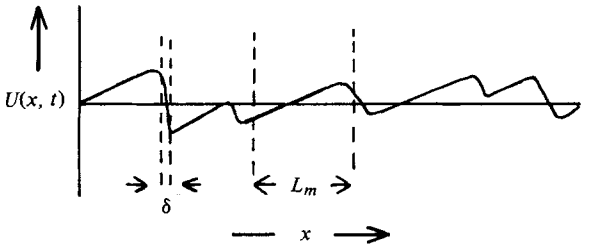

FIGURE 1. Typical velocity profile.

was set for the freely decaying ensembles at 16, 65, 180, 325, and for the stochastically forced ensemble at 500.

A second-order finite difference analogue of equation (1) was used to obtain the solutions reported below. Samples were taken from repeated realizations, and spectral variables were averaged over adjacent wavenumbers. It was found that a sample of 32 realizations allowed smooth and repeatable profiles to be obtained for the flow features of interest to this study. The salient features of the numerical model are the use of the implicit Crank–Nicholson time stepping procedure, an energy conserving space-differencing scheme for the nonlinear terms, and central space-differencing schemes for all the remaining terms. Both the stochastic forcing function and initial flow field were constructed by the Wiener process (Jeng 1969) to have Gaussian statistics with the power spectrum

$$Ak^4 \exp(-\tfrac{1}{2}k^2\sigma^2). \tag{27}$$

Here A and σ are constants: σ was selected such that the ratio $L/L_0 \sim 12$; this confined the velocity spectrum to approximately the first 50 wavenumbers. The values of A and ν were chosen to give the values of Re specified above, whilst still confining the dissipation specture to approximately the first 250 wavenumbers. The mesh interval h was set at $L/4096$, which was approximately $\frac{1}{8}$th of the smallest wavelength of significance. This choice means that aliasing errors and first and second derivative errors do not cause any appreciable distortion of the high wavenumber tail of the velocity spectrum.

3.2. *Exact dynamics*

Burgers' equation governs a one-dimensional flow in which fluid volume is not conserved. Figure 1 displays a typical velocity profile. Two characteristic lengths can be identified: a macroscopic length scale L_m associated with the energy containing modes, and a microscopic length scale δ, the shock front width, which is associated with the dissipation process; L_m will be of the same order as L_0 defined above while δ will vary inversely as Re (Jeng & Meecham 1972). Also both length scales will vary as the flow evolves in time. It is tempting to define an 'intrinsic' Reynolds number in terms of the ratio of these two lengthscales, and then to compare it with the corresponding ratio for Navier–Stokes turbulence. Unfortunately it turns out that this cannot be done in a self-consistent manner, and we therefore define the Reynolds number for Burgers' turbulence by equation (26). This is because Kolmogorov's hypothesis is not valid in one dimension; the small-scale structure of Burgers' turbulence is not a function of the dissipation rate ϵ and viscosity ν only.

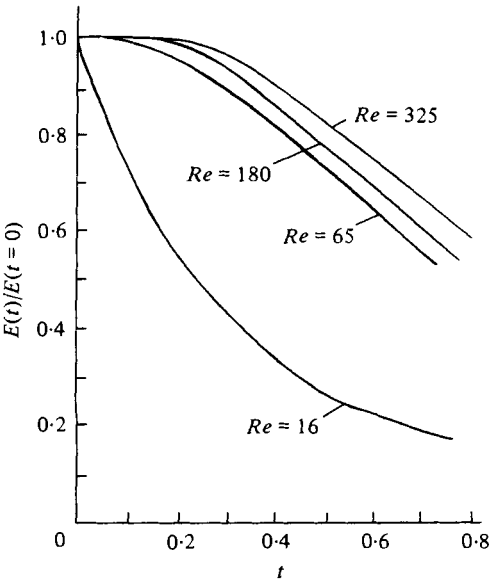

FIGURE 2. Variation of total energy with t and Re (free decay ensemble).

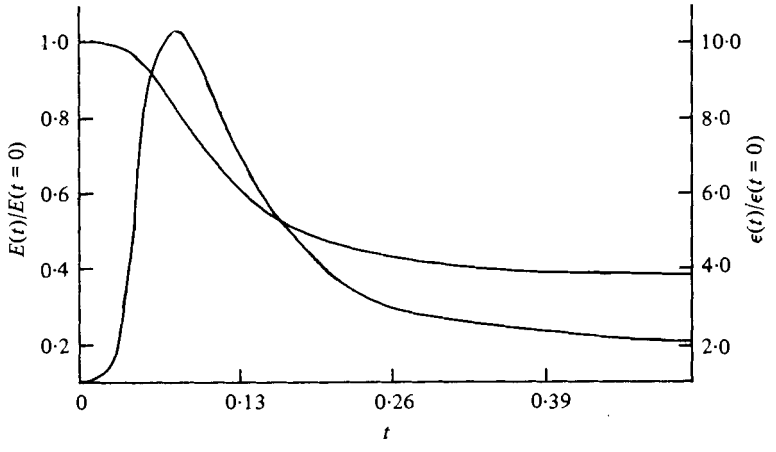

FIGURE 3. Time variation of total energy and dissipation (stochastically forced ensemble), $Re = 500$.

Plotted on figures 2 and 3 are the computed variation with time of both mean energy and mean dissipation per unit length for freely decaying and stochastically forced ensembles of flow fields at varying Re. For $Re \gtrsim 65$ these profiles display three distinct phases of evolution. For small t little dissipation of energy occurs. Next, for intermediate t the rate of dissipation increases sharply, and then finally for large t the flow either settles to an equilibrium level (for the stochastically forced ensemble) or drops off to zero (for the freely decaying ensemble). The interpretation of these observations is that in the first phase the more rapidly moving fluid particles overtake the slower moving ones, and shock fronts with the characteristic saw-tooth profile thus form.

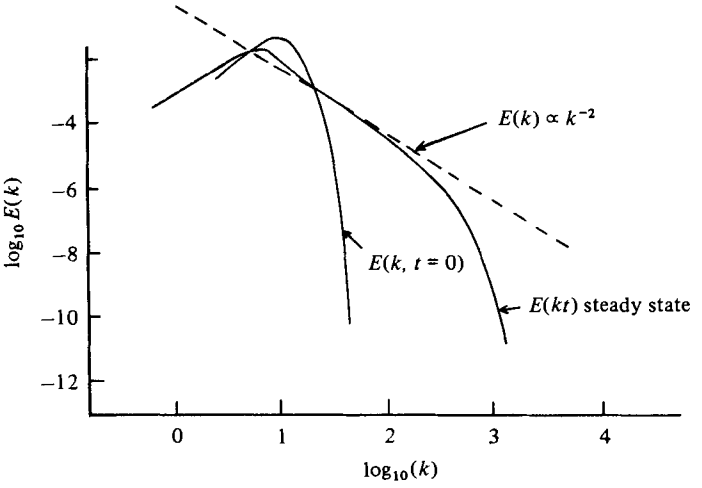

FIGURE 4. Initial and evolved velocity spectra (stochastically forced ensemble).

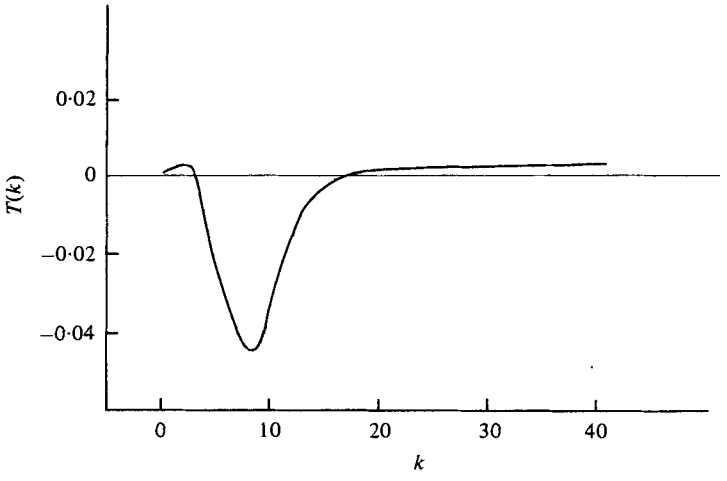

FIGURE 5. Transfer spectrum.

Little dissipation takes place during this phase, which is termed the pre-shock phase, since at high Reynolds numbers dissipation occurs predominantly in the shock fronts and these have yet to form. With the onset of shocks the flow evolves into the second or post-shock phase and regions of strong vorticity appear, which sweep in an intermittent manner across the flow field. Fluid volume is not conserved and the shocks, which move with the average velocity of the adjaecent fluid elements, coalesce on collision. The dissipation rate depends on the rate at which fluid particles are convected into the shocks, and thus the normalised dissipation rates shown on figure 2 are independent of Re. Although the width of the shock fronts or dissipation eddies is inversely proportional to Re, the characteristic profile of these eddies is independent of the large scale motions: these determine the number and evolution of the shocks. Thus for Burgers' model turbulence the large energy-containing eddies and small dissipation eddies are statistically independent.

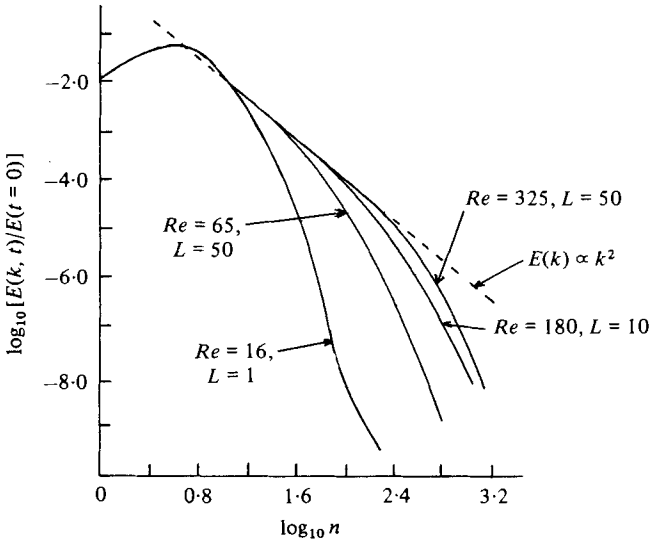

FIGURE 6. Evolved velocity spectra $K = 2n\pi/L$, $n = 0, 1, 2, \ldots$.

In the case of the freely decaying ensemble with $Re = 16$ the Reynolds number is sufficiently low that the viscous forces are important at all stages of the flow evolution. These forces oppose the formation of regions of steepened velocity gradient, and thus the mean energy of the flow drops off rapidly with time.

Equation (1) embodies an energy conserving cascade process (see also equation (25)) in which energy is transferred from low wavenumbers to high wavenumbers, where it is dissipated by viscous forces. Figures 4, 5 and 6 illustrate three different aspects of this process. Plotted on figure 4 are velocity spectra at different moments in time. The initial spectrum is confined to low wavenumbers. As the flow evolves higher and higher wavenumbers are excited, until the steady state spectral form is attained. Figure 5 shows the equilibrium transfer spectrum $T(k)$ for the stochastically forced ensemble: $T(k)$ (see equation (25)) represents the transfer of energy from wavenumber k to all other wavenumbers. It is seen that at low wavenumbers $T(k)$ is negative, representing a net outflow of energy to other wavenumbers, while at high wavenumbers it is positive representing a net gain. The integral of $T(k)$ over all wavenumbers is of course zero.

The post-shock evolved velocity spectra plotted on figure 6 are for freely decaying ensembles of flow fields at varying Re. These profiles together with figure 4 show that at intermediate wavenumbers the velocity spectrum is well fitted by a k^{-2} power law. This is analogous to the inertial range of Navier–Stokes turbulence, and shows Burgers' equation to conform to an important ingredient of Kolmogorov's inertial range theory.

The above findings demonstrate that there are many qualitative similarities between the dynamics of Burgers' turbulence and Navier–Stokes turbulence. We suggest that it is the existence of an inertial range at high Reynolds numbers and the statistical independence of the large and small scale flow features which make Burgers model turbulence a useful vehicle for exploring the sub-grid modelling techniques which are used in large-eddy simulations of the Navier–Stokes equations. Nevertheless caution must be exercised in interpreting our findings since there are important differences

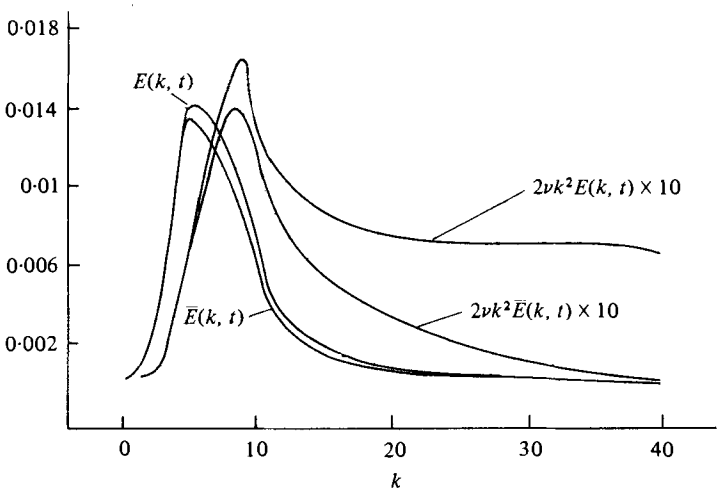

FIGURE 7. Exact and filtered spectra.

between the dynamics of the two flows. For example detailed study of figure 5 shows that for Burgers model turbulence a downward cascade of energy occurs at very low wavenumbers. The polarisation of energy towards lower and higher wavenumbers results from the tendency of the flow fields to organize themselves into regions of smooth variation of velocity gradient, together with isolated regions of steep velocity gradient (the shock fronts). This results in a precise ordering of phase of the low wavenumber components, an effect not found in Navier–Stokes turbulence. Burgers' equation thus reduces initial chaos instead of increasing it, an effect which is directly attributable to the absence of a pressure term. In turbulence pressure-induced accelerations cause fluid particles to forget the history of their motions and two flow fields which are initially almost identical will quickly diverge. In Burgers' turbulence loss of memory occurs only through the action of the viscous forces and random accelerations produced by the driving force, and in marked contrast to Navier–Stokes turbulence different realizations of the initial velocity fields driven by the same realization of the driving force converge. Another marked difference between Navier–Stokes turbulence and Burgers turbulence is seen from figures 6 and 7. The inertial range of Burgers turbulence displays a k^{-2} profile in contrast to the $k^{-\frac{5}{3}}$ inertial range profile of turbulence. This means that the post-shock dissipation spectra for Burgers' equation are flat throughout the inertial range. In Navier–Stokes turbulence the dissipation spectrum varies as $k^{+\frac{1}{3}}$.

3.3. *Filtered dynamics*

The velocity fields computed for the stochastically forced ensemble were spatially filtered using the Gaussian filter specified in equation (4) with $\Delta = L/64$. This filter (see figure 7) corresponds to the filter used for the large-eddy simulations reported in the next section. It retains about 80 % of the total energy and about 5 % of the dissipation, i.e. it weakly attenuates the velocity spectrum and strongly attenuates the molecular viscosity dissipation spectrum. Fig. 8 shows the time variation of mean energy per unit length for the filtered fields. It is seen that this profile does not display the sharp kink at $t \sim 60\Delta t$ shown by the exact fields (see figure 3). It will be recalled

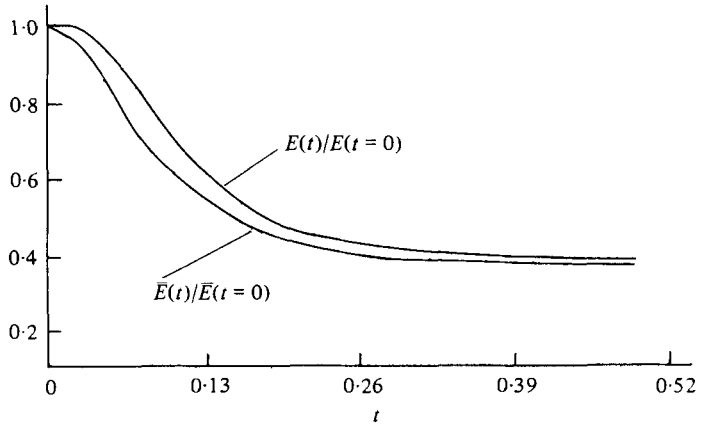

FIGURE 8. Time variation of total energy in filtered field.

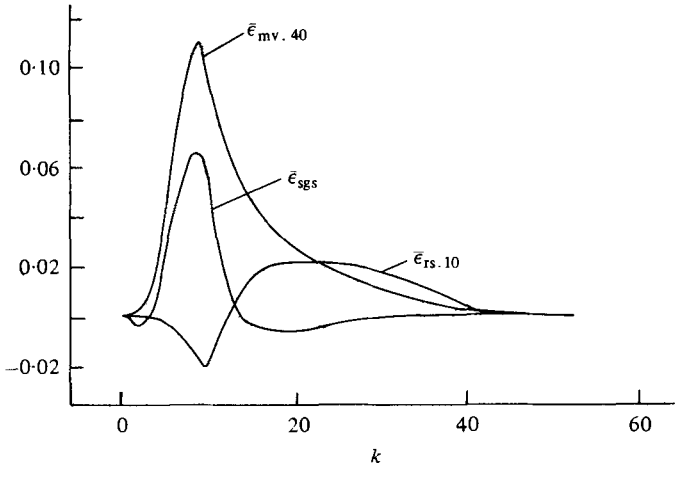

FIGURE 9. Subgrid dissipation components.

that this kink corresponds to the onset of shocks. Its absence in figure 8 is explained as follows. During the first stages of the evolution of the exact velocity fields little dissipation takes place as energy cascades from low wavenumbers to high wavenumbers. This energy is not lost and there is thus no net dissipation of energy from the exact fields. Ultimately sufficiently high wavenumbers are excited that the viscous forces begin to bite, and the dissipation rate then builds up. In contrast, during the first stages of the evolution of the filtered velocity fields this same cascade appears as a net dissipation, since the energy cascading out of the low wavenumbers represents a net loss of energy from the filtered fields and a net gain of energy by the subgrid velocity fields.

The spectral distribution of the components of the residual stress dissipation rate at $t = 1032\Delta t$ is plotted on figure 9. It is interesting to note that $\bar{\epsilon}_{rs}$ peaks at higher wavenumbers than $\bar{\epsilon}_{sgs}$, while $\bar{\epsilon}_{mv}$ has a high wavenumber tail. This suggests that $\bar{\epsilon}_{rs}$ and $\bar{\epsilon}_{mv}$ play an important role in controlling high-wavenumber excitations in large-eddy simulations. It is seen that $\bar{\epsilon}_{sgs}$ peaks near to the peak of $\bar{\epsilon}_{mv}$ which suggests that

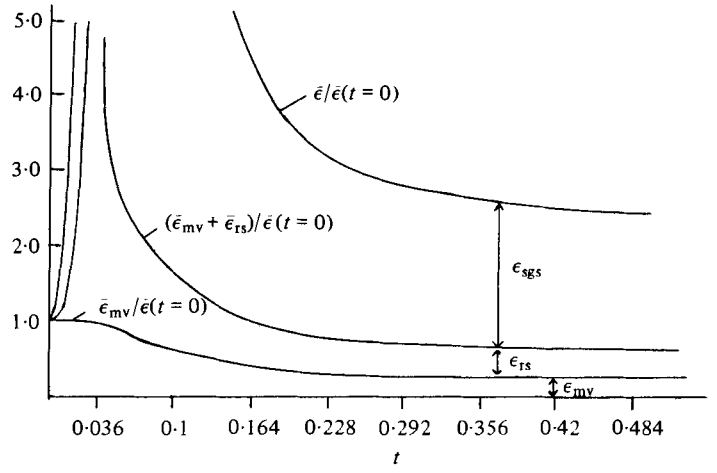

FIGURE 10. Time variation of components of residual stress dissipation rate.

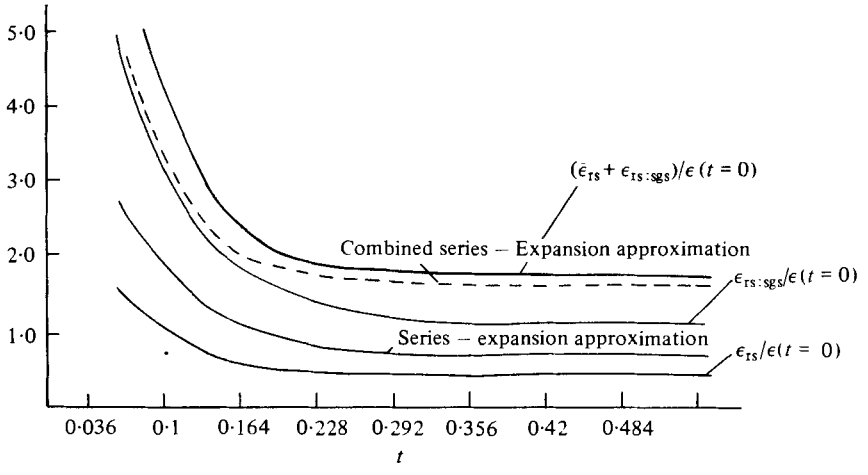

FIGURE 11. Time variation of approximations to $\bar{\epsilon}_{rs}$ and $\bar{\epsilon}_{rs:sgs}$

for the evolved velocity field $\bar{\epsilon}_{sgs}$ has a structure similar to that of $\bar{\epsilon}_{mv}$. The shape of the high-wavenumber tail of $\bar{\epsilon}_{mv}$ is influenced by the choice of filter. For example with $\Delta = L/32$ the tail is attenuated and $\bar{\epsilon}_{mv}$ approaches the shape of $\bar{\epsilon}_{sgs}$ quite closely. This suggests that the subgrid drain term in equation (5) can be usefully approximated by the eddy-viscosity model of equations (7), (11) (12) and (13). It further suggests that the approximation of treating the ν_{Ti} as independent of space (though dependent on time) is reasonable. These results support earlier unpublished findings of Leonard & Patterson for low Reynolds numbers freely decaying Navier–Stokes turbulence. Also the qualitative similarities between the profiles shown on figure 9 and corresponding profiles obtained by Leonard & Patterson suggest that the energy transfer between the grid and subgrid scales divides itself in a similar manner in the two flows.

Figure 10 shows the time variation of the components of the residual stress dissipation rate. It is seen that $\bar{\epsilon}_{rs}$ and $\bar{\epsilon}_{mv}$ account for approximately 20 % in total (10 % each) of the net dissipation in the filtered fields. Bearing in mind the predominance of

these terms at high wavenumbers this supports the view that they play an important role in controlling high wavenumber excitations in large eddy simulations.

The series approximations to $\bar{\epsilon}_{rs}$ and $\bar{\epsilon}_{rs:sgs}$ introduced in subgrid models 2 and 3 (see equations (21) and (22) make identical contributions to the mean energy balance per unit length in the filtered velocity fields. It can be seen from figure 11, where the computed time variations of these quantities are plotted, that although the contribution from the series approximations (dotted lines) predicts the magnitude and broad trend of both $\bar{\epsilon}_{rs}$ and $\bar{\epsilon}_{rs:sgs}$ correctly, it is in error by about 50 %. The approximation lies between $\bar{\epsilon}_{rs}$ and $\bar{\epsilon}_{rs:sgs}$; it overestimates $\bar{\epsilon}_{rs}$ and underestimates $\bar{\epsilon}_{rs:sgs}$. Interestingly enough the two series approximations combined together (broken line) give quite a reasonable approximation to the sum of $\bar{\epsilon}_{rs}$ and $\bar{\epsilon}_{rs:sgs}$. This suggests that subgrid model 3 may prove superior, though it should be remembered that the results presented in figure 11 provide only a very coarse measure of the performance of the different subgrid models.

4. Coarse-mesh calculations

4.1. *The numerical model*

Coarse-mesh calculations are reported and compared with exact solutions for two flow situations. In the first we attempt to reproduce on a coarse mesh the results of the fine-mesh calculations reported in § 3 for the stochastically forced ensemble of flow fields. In the second we solve (1) on a coarse mesh with $\nu = 0$ and

$$f(x,t) = A \sin 2\pi\{(x/L) - (t/T_0)\}, \tag{28}$$

where A denotes a constant. An exact solution to (1) exists for this case (Jeng 1969) which, if we scale all distances with L and all times with T_0, takes the form

$$\begin{aligned} u(x,t) &= 1 + (2A/\pi)^{\frac{1}{2}} \sin(\pi(x-t)), \quad 0 \leqslant x \leqslant x_s, \\ &= 1 - (2A/\pi)^{\frac{1}{2}} \sin(\pi(x-t)), \quad x_s < x \leqslant 1. \end{aligned} \tag{29}$$

This solution describes a discontinuous travelling wave which sweeps periodically across the flow field. The location of the discontinuity x_s is determined by the condition

$$\int_0^1 u(x,t)\,dx = 1 - (2\pi)^{\frac{3}{2}} A^{\frac{1}{2}} \cos(\pi(x_s - t)) = 0 \tag{30}$$

while the speed at which the shock fronts propagate is given by the average velocity of the adjacent fluid elements. This exact solution provides a more accurate standard of comparison for the coarse mesh calculations than do the fine mesh calculations of § 3.

A fourth-order finite difference scheme was used for these calculations. This is because the series expansions used in § 2.2 suggest that the residual stress terms are of $O(\Delta^2)$, where $\Delta \sim h$ the mesh interval. This in turn implies that a difference scheme accurate to at least $O(h^2)$ is necessary if the residual stress terms are to remain more significant than differencing errors.

Since there are many disadvantages to fourth-order difference schemes many workers in the field now question whether in practice schemes accurate to the second order might suffice. Fourth-order schemes are more complex to implement than

second-order schemes, which leads to a sizeable increase in run times, they spread over more mesh points than second order schemes thus making the treatment of boundaries more difficult, and they require a smaller time step than second-order schemes to avoid time differencing instability. There are in any case doubts about the convergence of the expansions introduced in § 2.2 and thus doubts that the residual stress terms are of $O(\Delta^2)$. Taking the Fourier transform of equation (2) we find

$$\bar{g}(k,t) = G(k)\, g(k,t), \tag{31}$$

whence

$$g'(k,t) = \left[\frac{1-G(k)}{G(k)}\right] \bar{g}(k,t) \tag{32}$$

$$= -\left[\frac{\Delta^2}{24} k^2 + O(\Delta^4 k^4)\right] g(k,t) \tag{33}$$

for the Gaussian filter. Here $G(k)$, $\bar{g}(k)$ and $g(k)$ denote the transforms of $G(x)$, $\bar{g}(x)$, and $g(x)$ respectively while $k = 2n\pi/L$. This expansion is valid for $\Delta k \ll 1$ but is not convergent for $\Delta k > 1$. The results set out in § 3.3 show that the residual stress terms peak at wavenumbers where $\Delta k > 1$, and indeed suggest that the expansions are poor approximations. It has therefore been suggested (Shaanan, Ferziger & Reynolds 1975) that second-order difference schemes might prove to be equally satisfactory provided that they are chosen so that their truncation errors match to a good approximation the resolvable scale component of the residual stress term.

For example

$$[\bar{u}(x+h) + \bar{u}(x) + \bar{u}(x-h)]\,[\bar{u}(x+h) - \bar{u}(x-h)]/6h$$

$$= \bar{u}\frac{\partial}{\partial x}\bar{u} + \frac{h^2}{6}\bar{u}\frac{\partial^3 \bar{u}}{\partial x^3} + \frac{h^2}{3}\frac{\partial}{\partial x}\bar{u}\frac{\partial^2}{\partial x^2}\bar{u} + O(h^4) \tag{34}$$

$$= \frac{1}{2}\frac{\partial}{\partial x}\left[\bar{u} + \frac{h^2}{6}\frac{\partial^2}{\partial x^2}\bar{u}^2 - \frac{h^2}{6}\left(\frac{\partial \bar{u}}{\partial x}\right)^2\right] + O(h^4). \tag{35}$$

The left-hand side of (34) is a energy-conserving finite-difference approximation to the term $\bar{u}\,\partial\bar{u}/\partial x$ accurate to the second order. Alternatively the right-hand side of (35) can be regarded as the basis for another different subgrid model. Pursuing this argument we approximate R as

$$R = \frac{h^2}{12}\frac{\partial^2}{\partial x^2}\bar{u}^2 - \frac{h^2}{12}\left(\frac{\partial}{\partial x}\bar{u}\right)^2 - \nu_{T4}\frac{\partial}{\partial x}\bar{u}, \tag{36}$$

where ν_{T4} is the turbulent viscosity introduced in (13).

4.2. *Calculations of the subgrid constants*

The values of the subgrid constants used in the coarse mesh calculations reported below were obtained by a trial and error approach. Initially selected values for the c_i were adjusted until the steady-state value of the mean energy per unit length in the coarse-mesh calculation (i.e. $\bar{E}(t)$) agreed with the corresponding quantity taken from the exact calculations. Figure 12 illustrates this process for the stochastically forced ensemble while the results of some of the calculations are given in table 1.

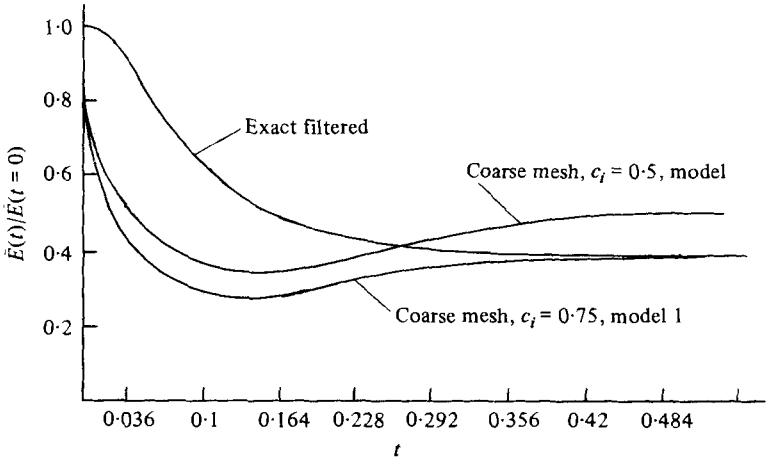

FIGURE 12. Time variation of energy in coarse-mesh calculation.

Flow	Sub-grid model	Δ	W	h	c_i	Δt
Travelling wave	1	$L/64$	0	$L/128$	0·9	0·001
	2	$L/64$	0	$L/128$	0·8	0·001
	3	$L/64$	0	$L/128$	0·7	0·001
Stochastic ensemble	1	$L/64$	$L/16$	$L/128$	0·8	0·008
	2	$L/64$	$L/16$	$L/128$	0·8	0·008
	3	$L/64$	$L/16$	$L/128$	0·7	0·008
	2	$L/32$	0	$L/128$	0·3	0·002
	2	$L/128$	0	$L/128$	2·0	0·002
	2	$L/64$	0	$L/128$	0·8	0·002
	2	$L/64$	$L/32$	$L/128$	0·7	0·004
	2	$L/64$	$L/128$	$L/128$	0·7	0·004

TABLE 1. Subgrid constants: Δ = filter width; W = eddy viscosity averaging length scale; h = mesh interval; c_i = eddy-viscosity constant.

It is seen from figure 12 that for the stochastically forced ensemble the coarse-mesh calculations overestimate the rate of loss of energy during the first stages of the flow's evolution, and then gradually return to an equilibrium level. This pattern was observed for each of the subgrid models studied, and was also observed for the travelling wave solution when these calculations were started using as initial conditions velocity fields that were not similar to the equilibrium velocity profile. This phenomenon may be related to the tendency of the turbulence to collapse which Moin, Reynolds & Ferziger (1978) encountered in their simulation of channel flow. It demonstrates that the subgrid modelling is only successful in situations where a fully developed inertial range spectrum exists. The corollory of this is that the subgrid modelling misrepresents the subgrid energy drain during the first stages of the flow's evolution. This is because the initial velocity spectrum is confined to low wavenumbers and thus for the exact fields the $u'(x, t = 0)$ and consequently $\bar{\epsilon}_{sgs}(t = 0)$ are zero, while for the coarse-mesh

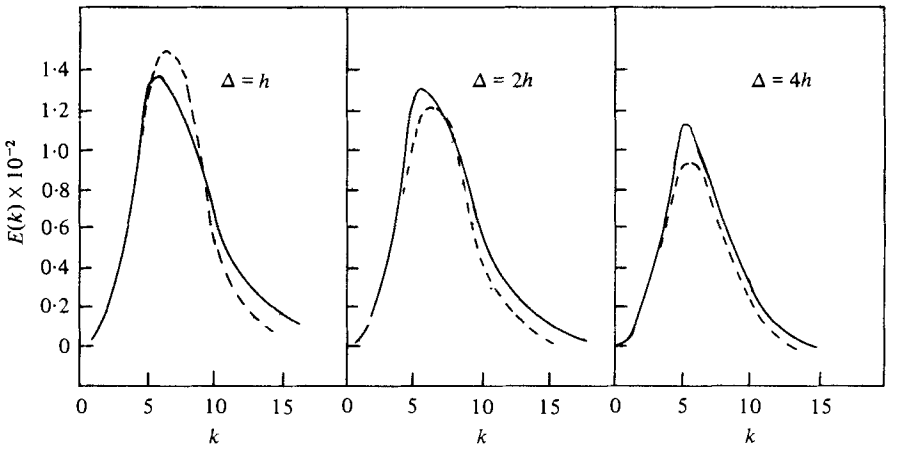

FIGURE 13. Exact-filtered and coarse-mesh velocity spectra: ---, coarse mesh; ——, exact filtered.

calculations the subgrid model represents the u' in terms of the $\bar{u}(x,t)$ which are not zero. Consequently in the coarse mesh calculations $\bar{\epsilon}_{\rm sgs}(t=0)$ is substantially positive, and the coarse-mesh calculations thus overestimate the initial rate of loss of energy.

The results presented in table 1 for the c_i are accurate to at least 5 %: they were not determined to a higher accuracy simply because of the time-consuming nature of the adjustment procedure. It can be seen that the c_i are not too sensitive either to the differences between the two flows or to the eddy viscosity averaging length scale W. This is because any variation in W influences primarily the high wavenumbers (see figure 16), while figure 9 shows that the subgrid dissipation in a coarse-mesh calculation is determined primarily by the low wavenumbers. However the c_i decrease as Δ is increased. This is because as Δ increases so the amount of energy included in the coarse mesh calculation decreases. Finally we note that the tendency for $c_1 > c_2 > c_3$ is as one would expect since in subgrid model 1 the eddy viscosity term has to cope with the whole of the energy drain.

4.3. *Optimization of filter width and eddy viscosity averaging length*

The profiles plotted on figure 13 are the exact filtered and coarse mesh velocity spectra obtained from three stochastically forced ensemble calculations using subgrid model 2 and with $\Delta = h$, $2h$, and $4h$, $h = L/128$, $W = 0$ and $\Delta t = 0{\cdot}008$. In each case the calculation was carried forward in time for a further 50 time steps to check that the displayed spectrum has evolved to a stationary state. It is seen that the coarse-mesh calculations all reproduce the shape of the filtered fine-mesh velocity spectra at low wavenumbers quite accurately. The differences in area between the filtered fine mesh and coarse-mesh fields are not significant. This is because the area under each curve is a measure of the total energy in the coarse mesh and filtered fine-mesh fields, and these two quantities have been brought into close agreement by tuning the subgrid constants c_i.

The plots of $\log_{10}\bar{E}(k)$ against k in figures 14 and 15 are for the stochastically forced ensemble and the travelling-wave solution. They show that in all cases the coarse-

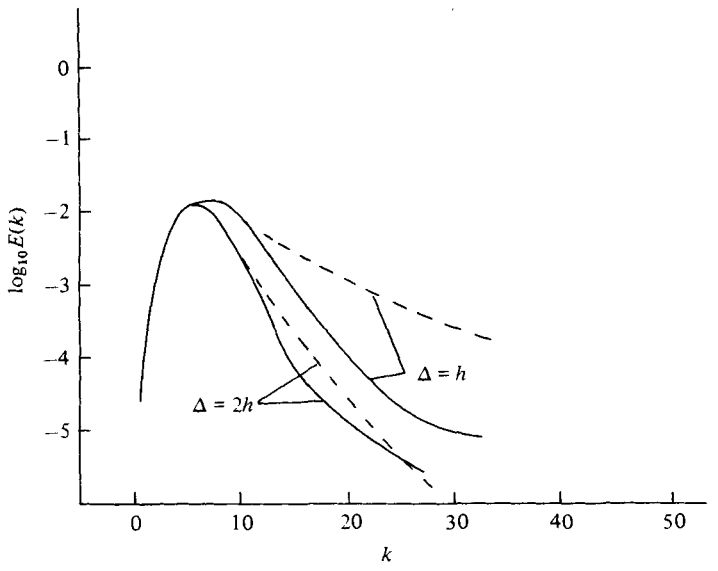

FIGURE 14. Coarse-mesh and exact-filtered velocity spectra: ——, coarse mesh; – – –, exact filtered.

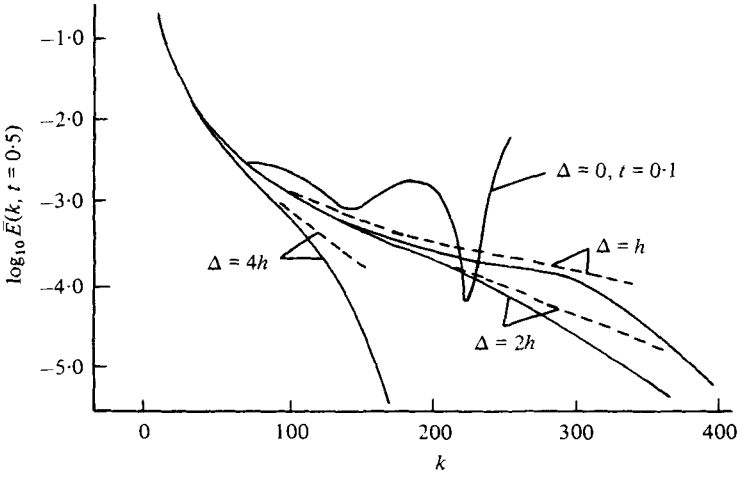

FIGURE 15. Coarse-mesh velocity spectra, variable filter width: ——, coarse mesh; – – –, exact filtered.

mesh calculations over-attenuate the high wavenumber velocity spectrum. They also suggest that $\Delta \sim 2h$ is roughly the optimum, since this choice gives fairly close agreement between the coarse-mesh and exact-filtered profiles at high wavenumbers, while still retaining 80 % of the total energy. This conclusion supports the earlier findings of Kwak *et al.* (1975). The profile for $\Delta = 0$ shown in figure 15 is equivalent to the result of a calculation in which the residual stress terms of (5) are ignored. The gross distortion and erratic behaviour of the computed velocity spectrum at high wavenumbers for this case shows very clearly the need for subgrid modelling. In the absence of the subgrid drain term there is no mechanism for dissipating the energy which is trans-

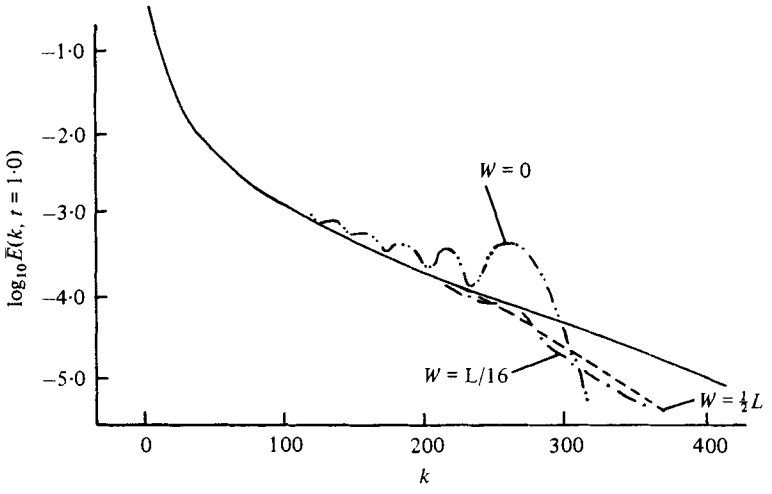

FIGURE 16. Coarse-mesh velocity spectra, comparison of eddy viscosities: ---, —·—, —··—, coarse mesh; ——, exact filtered.

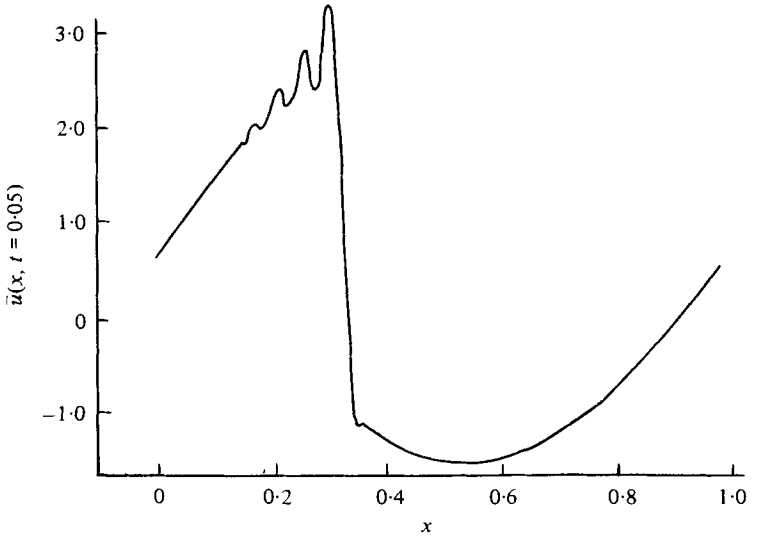

FIGURE 17. Coarse-mesh velocity field, model 2, $W = 0$, $h = L/256$, $\Delta = L/32$.

ferred by the non linear inertial forces from low wavenumbers to high wavenumbers. The consequence of this is the pile-up observed at the high wavenumber end of the spectrum, and ultimately a breakdown in the computation.

The computations leading to figure 15 were repeated with W varying from 0 to $\frac{1}{2}L$. It is seen from figure 16 that a marked improvement occurs in the coarse-mesh calculation when $W = 4\Delta$, and that for the case of $W = 0$, i.e. the Smagorinsky subgrid model, the coarse-mesh spectrum displays oscillations at high wavenumbers. These results favour the Direct Interaction or non-local subgrid model (Love & Leslie 1977).

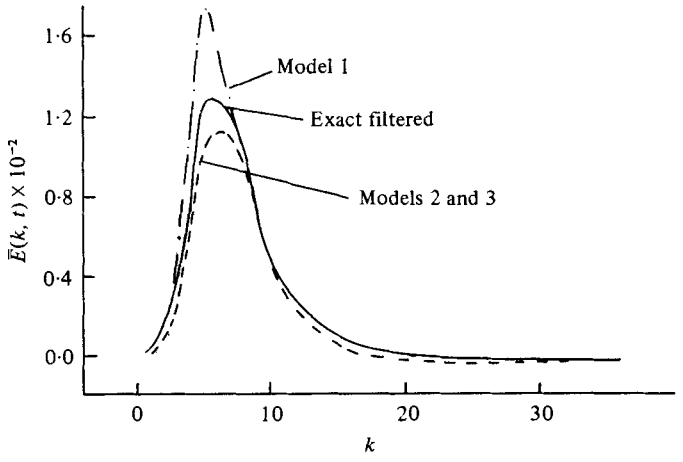

FIGURE 18. Coarse-mesh velocity spectra.

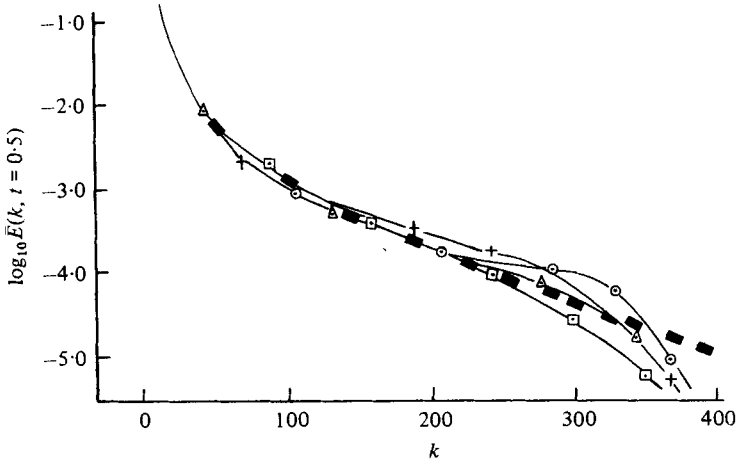

FIGURE 19. Coarse-mesh velocity spectra, comparison of residual-stress models 1(△), 2(⊡), 3(⊙) and 4(+). ■, exact-filtered spectrum.

A more detailed numerical study of the time evolution of the oscillations observed for $W = 0$ shows that they grow from small disturbances appearing initially at the highest wavenumbers. Figure 17 shows that these disturbances manifest themselves in configuration space as small shocks located along the trailing edge of the main shock front. There are no small shocks along the leading edge of the main shock because as the main shock sweeps across the flow it overtakes and engulfs any flow perturbations that move out along its leading edge. Love & Leslie (1977) have suggested the following explanation of these observations. In a coarse-mesh calculation a local eddy viscosity coefficient causes small distortions moving out from the main shock fronts to evolve into smaller shocks. These distortions, which are due to misrepresentation of the subgrid drain terms by the subgrid model, are found to have a characteristic length

scale of $O(3\Delta)$. The resulting subsidiary shocks can be regarded as a genuine but unwanted feature of the coarse-mesh solution. Averaging the eddy viscosity over a length $W \sim 4\Delta$ inhibits their formation because this makes the eddy viscosity insensitive to small flow perturbations.

It was found in the coarse-mesh calculations for the stochastically forced ensemble of flow fields that varying W had only a marginal effect on the high wavenumber tail of the computed velocity spectra. This is as expected since the chaotic nature of these flows means that small perturbations of the above type will be removed during the normal ensemble averaging operation, and will therefore not affect the displayed velocity spectra. Consequently this investigation does not imply that a non-local eddy viscosity will necessarily be superior to a local one for the Navier–Stokes equations. It is likely that it will only be superior in situations where the detailed evolution of individual flow features is of interest.

4.4. *Comparison of subgrid models*

Comparing the results of coarse-mesh calculations using models 1 through 4 shows that there is very little in practice to choose between the subgrid models in so far as the prediction of ensemble average flow features is concerned. The spectra shown on figures 18 and 19 are all equilibrium spectra: for the calculations on the stochastically forced ensemble (figure 18) we set $\Delta = 2h = L/64$, $\Delta t = 0{\cdot}008$ and $W = L/16$, while for the calculations on the travelling-wave solution (figure 19) we set $\Delta = 2h = L/64$, $\Delta t = 0{\cdot}001\ T_0$ and $W = L$. It is seen from both figures that all models reproduce the low wavenumber velocity spectrum quite accurately; again the reader is reminded that the differences in area under the curves are not significant (see §4.3). Model 4 is perhaps the least satisfactory. It predicts a slight shift in the peak of the velocity spectrum shown on figure 18, while on figure 19 it underestimates the velocity spectrum at both low and high wavenumbers and overestimates it at intermediate wavenumbers. Figure 19 shows that at high wavenumbers all models misrepresent the velocity spectrum. Model 2 gives perhaps the best representation, though this is marginal. For the stochastically forced ensemble all models underestimate the velocity spectrum at high wavenumbers and predict profiles similar to those shown on figure 14.

This similarity between the subgrid models in predicting gross flow features is not too surprising, and is explained thus. In the exact solutions to Burgers' equation the bulk of the dissipation occurs in the shock fronts, which are regions of high velocity gradient. Elsewhere the velocity gradient has a small positive value. This means that at high Re large values of the derivative $\partial u/\partial x$ only occur when the sign is negative, thus implying that to close approximation the equation

$$\langle(\partial u/\partial x)^3\rangle \doteq \langle -|\partial u/\partial x|(\partial u/\partial x)^2\rangle \tag{37}$$

holds true. The coarse-mesh velocity solutions are broadly similar to the fine-mesh velocity solutions, and it can be likewise argued that, despite the tendency of the resolvable scale terms to smooth regions of steepened velocity gradient, the large values of $\partial\bar{u}/\partial x$ will still have one sign: negative. Accordingly the relation

$$\langle(\partial\bar{u}/\partial x)^3\rangle \doteq \langle -|\partial\bar{u}/\partial x|(\partial\bar{u}/\partial x)^2\rangle \tag{38}$$

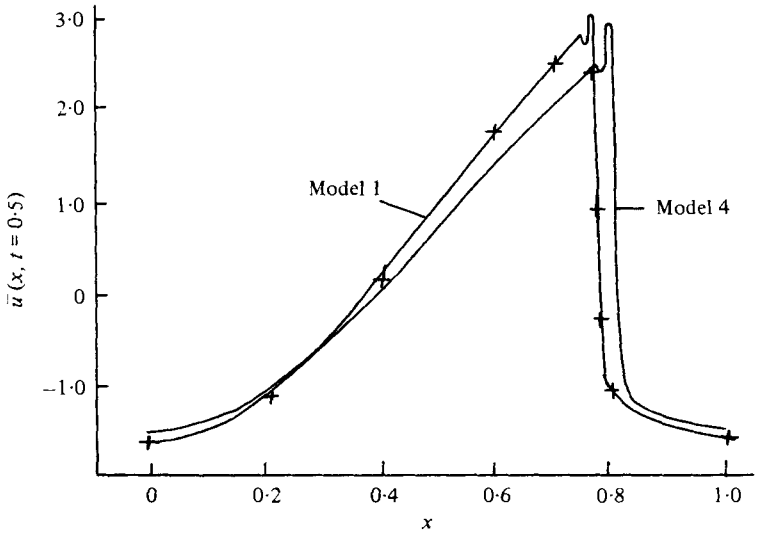

FIGURE 20. Coarse-mesh velocity field. +, exact-filtered field.

will also hold, but not so accurately as (37). It follows then that for each model the contribution of the residual stress term to the energy balance in the coarse-mesh calculation is as follows:

$$\text{Model 1} \quad \left\langle \bar{u}\frac{\partial R}{\partial x}\right\rangle \doteq \Delta^2 c_1^2 \left\langle \left|\frac{\partial \bar{u}}{\partial x}\right| \left(\frac{\partial \bar{u}}{\partial x}\right)^2 \right\rangle; \tag{39}$$

$$\text{Model 2} \quad \left\langle \bar{u}\frac{\partial R}{\partial x}\right\rangle \doteq \Delta^2 (c_2^2 + \tfrac{1}{48}) \left\langle \left|\frac{\partial \bar{u}}{\partial x}\right| \left(\frac{\partial \bar{u}}{\partial x}\right)^2 \right\rangle; \tag{40}$$

$$\text{Model 3} \quad \left\langle \bar{u}\frac{\partial R}{\partial x}\right\rangle \doteq \Delta^2 (c_3^2 + \tfrac{1}{24}) \left\langle \left|\frac{\partial \bar{u}}{\partial x}\right| \left(\frac{\partial \bar{u}}{\partial x}\right)^2 \right\rangle; \tag{41}$$

$$\text{Model 4} \quad \left\langle \bar{u}\frac{\partial R}{\partial x}\right\rangle \doteq \Delta^2 c_4^2 \left\langle \left|\frac{\partial \bar{u}}{\partial x}\right| \left(\frac{\partial \bar{u}}{\partial x}\right)^2 \right\rangle. \tag{42}$$

This shows why the predictions of the mean energy per unit length are so similar for all 4 models. It also implies

$$c_1^2 \simeq c_4^2$$
$$c_1^2 > c_2^2 > c_3^2$$

all of which relations were found to hold to within the accuracy of the computations (see table 1 and figure 19). I am indebted to a referee for this clarifying comment.

These results suggest that if we are interested in gross flow features only, subgrid model 4 would seem a reasonable compromise provided we are prepared to trade some loss of accuracy for a considerable simplification of the numerics. However, figure 20 shows that for the travelling-wave solution the coarse-mesh velocity field obtained with subgrid model 4 deviates considerably from the exact filtered field. Thus if we are particularly interested in the detailed evolution of a single realisation of a coarse-mesh calculation (e.g. weather forecasting) figures 19 and 20 suggest that subgrid models 1 and 2 are preferable. The choice between models 1 and 2 depends upon the

price we are prepared to pay in computing time for the moderate improvement in accuracy which model 2 offers over model 1.

Finally, we remark that comparisons between the rate of change of total energy in the coarse mesh and exact filtered fields for a single realization of the stochastically forced ensemble calculation imply that the coarse mesh field over-responds to the driving force. Unfortunately due to large sampling errors this observation could not be conclusively established. If it is correct it means that in the coarse mesh calculations there is an excess injection of energy at low wavenumbers. Increasing the subgrid constant increases the low wavenumber dissipation rate, and thus returns the total energy to the correct equilibrium value. This also increases the dissipation at high wavenumbers, which are not being excited directly by the driving force, and thus would explain the excess attenuation of the high wavenumber tail observed in figure 14.

5. Conclusions

It has been confirmed that direct numerical solution of Burgers' equation is feasible at high *Re* and that the overall dynamics are not too unlike those of the Navier–Stokes equations. It is well known that the energy flow in the inertial range is towards higher wavenumbers in both systems. This study shows that the division of the drain from large to small eddies between the SGS and RS terms, and the structures of these terms, are also remarkably similar. This suggests that conclusions about subgrid modelling drawn from Burgers' equation should be reasonably applicable to the Navier–Stokes equations.

The coarse-mesh calculations confirm the need for subgrid modelling. The effectiveness of this technique has been tested in detail by comparing the coarse mesh calculations with filtered fine-mesh calculations. The standard Smagorinsky representation proves to be very satisfactory provided that the equation is prefiltered, the optimum filter width being about twice the mesh spacing. (Stanford workers have found a similar result for the Navier–Stokes equations.) Four different subgrid models of Smagorinsky type have been tested. They are all from the same vein as variants of the Smagorinsky subgrid model that have been used elsewhere in large eddy simulations of Navier–Stokes turbulence. It is demonstrated that the modifications to the basic Smagorinsky model embodied in the varients are (for Burgers' equation) essentially trivial and have little net effect on the computation of gross flow features. The modifications are however found to have some effect on the detailed structure of the computed flow fields. Detailed study of these effects leads to the conclusion that the simple Smagorinsky subgrid model with or without the Leonard variant is superior to the more complex forms derived from it. It is therefore recommended as the most satisfactory of the subgrid models investigated.

It has also been shown that for Burgers' equations the non-local (spatially averaged) eddy viscosity suggested by the classical closures is superior to the local variety. However, this result appears to depend on a shock propagation phenomenon particular to Burgers' equation, and it cannot be concluded without testing that the same result would hold for the Navier–Stokes equations.

The investigation has shown how error propagation at high wavenumbers can reduce the effectiveness of large eddy simulations, and has underlined the importance of controlling this phenomenon.

I am much indebted to Professor D. C. Leslie for his encouragement of this work and for many useful and lively discussions. His comments and those of the referees have also added substantially to the style and content of this paper.

This work was supported by S.R.C. under grant B/RG/3559.

REFERENCES

CORRSIN, S. 1961 Turbulent flow. *American Scientist* **49**, 300.

FERZIGER, J. H. 1976 Large eddy numerical simulations of turbulent flows. *A.I.A.A. paper* 76-347.

HOSOKAWA, H. & YAMAMOTO, K. 1975 Turbulence in the randomly forced, one dimensional Burgers flow. *J. Stat. Phys.* **13**, 245.

JENG, D.-T. 1969 Forced equation model for turbulence. *Phys. Fluids* **12**, 2006.

JENG, D.-T. & MEECHAM, W. C. 1972 Solution of forced Burgers' equation. *Phys. Fluids* **15**, 504.

KRAICHNAN, R. H. 1968 Lagrangian-history statistical theory for Burgers' equation. *Phys. Fluids* **11**, 265.

KWAK, D., REYNOLDS, W. C. & FERZIGER, J. H. 1975 Three-dimensional time dependent computation of turbulent flow. *Stanford Univ. Rep.* TF-5.

LEONARD, A. 1974 Energy cascade in large-eddy simulations of turbulent fluid flows. *Adv. Geophys.* **18**A, 237.

LESLIE, D. C. & QUARINI, G. L. 1979 The application of classical closures to the formulation of subgrid modelling procedures. *J. Fluid Mech.* **91**, 65.

LILLY, D. K. 1966 On the application of the eddy viscosity concept in the inertial sub-range of turbulence. *N.C.A.R. Rep.* no. 123.

LILLY, D. K. 1967 The representation of small-scale turbulence in numerical simulation experiments. *Proc. I.B.M. Scientific Computing Symp. on Environ. Sci.* 1966.

LOVE, M. D. & LESLIE, D. C. 1977 Studies of subgrid modelling with classical closures and Burgers' equation. *Proc. Symp. Turbulent Shear Flows, Univ. Park, PA.*

MOIN, P., REYNOLDS, W. C. & FERZIGER, J. H. 1978 Large eddy simulation of incompressible turbulent channel flow. *Thermosciences Division, Dept. of Mech. Engng* TF-12. Stanford University.

SHAANAN, S., FERZIGER, J. H. & REYNOLDS, W. C. 1975 Numerical simulation of turbulence in the presence of shear. *Stanford Univ. Rep.* TF-6.

SMAGORINSKY, J. S. 1963 General circulation experiments with the primitive equations. I. The basic experiment. *Mon. Weather Rev.* **91**, 99.